Short communication

A detailed $CO_2(^1B_2)$ chemiluminescence chemical kinetics model for carbon monoxide and hydrocarbon oxidation

Yushuai Liu [a,b,*], Yannis Hardalupas [b], Alexander M.K.P. Taylor [b]

[a] *Institute of Engineering Thermophysics, Chinese Academy of Sciences*
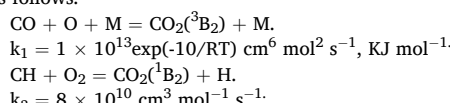[b] *Mechanical Engineering Department, Imperial College London*

ABSTRACT

The $CO_2(^1B_2)$ - $CO_2(X^1\Sigma_g^+)$ transition is a source of chemiluminescence from CO and hydrocarbon premixed flames and can be used as a diagnostic; however, its chemistry is not well known due to its broadband nature. Although several attempts have been made to model $CO_2(^1B_2)$ chemiluminescence, none performs well in hydrocarbon flames. We propose a new detailed kinetic model for $CO_2(^1B_2)$ chemiluminescence, based on shock tube experiments in the literature and on opposed flame data presented here. The mechanism consists of 26 reactions which describe the formation of the lower excited state molecule $CO_2(^3B_2)$ (R1), the inter-system crossing reaction between $CO_2(^3B_2)$ and $CO_2(^1B_2)$ (R2), $CO_2(^1B_2)$, the formatting reaction path in hydrocarbon flames (R3), $CO_2(^1B_2)$ radiative quenching (R4) and collisional quenching of $CO_2(^3B_2)$ and $CO_2(^1B_2)$ (R5-R26). The reaction rates constants of R1 and R3 within $\pm$ 60% and $\pm$ 32% uncertainty, respectively, were determined as follows:

$CO + O + M = CO_2(^3B_2) + M$.
$k_1 = 1 \times 10^{13}exp(-10/RT)$ cm^6 mol^2 s^{-1}, KJ mol^{-1}.
$CH + O_2 = CO_2(^1B_2) + H$.
$k_3 = 8 \times 10^{10}$ cm^3 mol^{-1} s^{-1}.

The mechanism was evaluated against several shock tube experiments at low and elevated pressures and also the $CO_2(^1B_2)$/OH* chemiluminescent intensity ratio for premixed CH_4-air and C_3H_8-air opposed flames measured in the current study. The comparison showed good agreement for $CO_2(^1B_2)$ temporal profiles for CO-based, CH_4-based and C_2H_4-based mixtures. The prediction of temperature dependence of the $CO_2(^1B_2)$ peak intensity for the CH_4-based mixture at both low and elevated pressures was much improved relative to previous models. The $CO_2(^1B_2)$/OH* chemiluminescent intensity ratio for premixed CH_4-air flames predicted by the new model agrees quite well with experiment data, while a small discrepancy remains for C_3H_8-air flames. Overall, the developed $CO_2(^1B_2)$ chemiluminescence model reproduces, a wide range of experimental data and extends knowledge of $CO_2(^1B_2)$ chemistry.

1. Introduction

Chemiluminescence can provide the basis of simple, nonintrusive instruments [1–5]: the intensities from OH($A^2\Sigma^+$-$X^2\Pi$), CH($A^2\Delta$- $X^2\Pi$), $C_2(d^3\Pi$-$a^3\Pi)$, and $CO_2(A^1B_2$- $X^1\Sigma_g^+)$ can monitor heat release rate and equivalence ratio [6–8]. The chemistry of prominent *narrowband* chemiluminescence, including OH(A) [9–11] at 309 nm, CH(A) [9,10] at 431 nm and C_2(d) [2,12] at 516 nm, has been extensively studied. In carbon monoxide and hydrocarbon flames [8,13–17], chemiluminescence of $CO_2(^1B_2)$ is believed to be the main source of the

broadband emission from 220 nm to 700 nm and also contributes to measured OH(A) and CH(A) intensities [5,8] for methane flames. In ultra-lean combustors and inert gas diluted, hydrogen enriched methane and syngas flames, $CO_2(^1B_2)$ is the main source of chemiluminescence and has been used to monitor equivalence ratio (φ) [7,18], dilution level [19] and heat release rate [1]. A detailed kinetic mechanism of $CO_2(^1B_2)$ chemiluminescence could guide quantitative interpretation and accurate evaluation of OH(A), CH(A) and C_2(d) chemical kinetic mechanisms.

The chemistry of its formation, radiative quenching and collisional

quenching is still debated. The detailed chemistry [14] in CO + H_2 flames includes three steps: CO + O + M = $CO_2(^1B_2)$ + M (R39), $CO_2(^1B_2)$ + M = CO_2 + M (R16-R26), and $CO_2(^1B_2)$ → CO_2 + hν (R4). Since direct formation of $CO_2(^1B_2)$ from CO + O is spin forbidden, a spin reversal process between $CO_2(^3B_2)$ and $CO_2(^1B_2)$ is needed and the mechanism for $CO_2(^1B_2)$ chemiluminescence in CO based flames was extended to include the reaction for $CO_2(^3B_2)$ formation and intersystem crossing reaction between $CO_2(^1B_2)$ and $CO_2(^3B_2)$. This scheme [20] is: CO + O + M = $CO_2(^3B_2)$ + M (R1), $CO_2(^3B_2)$ → $CO_2(^1B_2)$ (R2), $CO_2(^1B_2)$ → CO_2 + hν (R4), $CO_2(^3B_2)$ + M = CO_2 + M (R5-R15), and $CO_2(^1B_2)$ + M = CO_2 + M (R16-R26).

It is hard to isolate every reaction rate constant in these two detailed chemical schemes; literature tends to use a global mechanism for $CO_2(^1B_2)$ chemiluminescence: CO + O = CO_2 + hν (R0). The $CO_2(^1B_2)$ chemiluminescent intensity can be calculated by $I_c = k_0 \times$ [CO][O], where I_c is the $CO_2(^1B_2)$ chemiluminescent intensity, k_0 is the rate constant of (R39), and [CO] as well as [O] are the concentrations of CO and O respectively. A comprehensive review of k_0 can be found in [21]. All reaction rates for the overall $CO_2(^1B_2)$ chemiluminescence mechanism were calibrated in CO based mixture flames, leading to good agreement with experiments in CO flames. However, two shock tube measurements showed that the $CO_2(^1B_2)$ global mechanism for chemiluminescence is not able to represent the $CO_2(^1B_2)$ chemiluminescence time history in methane [22] and ethylene [17] mixtures.

Towards the detailed $CO_2(^1B_2)$ chemiluminescence mechanism, Kopp *et al.* [23] proposed a detailed $CO_2(^1B_2)$ chemiluminescence mechanism based on the first CO-O reaction scheme (R39, R16-26 and R4) (note as PG1) and further improved the reaction rate constant of R39 in 2015 [16] (note as PG2). The finalized reaction mechanism also included an HCO + O = $CO_2(^1B_2)$ + H reaction, as the $CO_2(^1B_2)$ generation path in hydrocarbon oxidation. This PG2 mechanism has shown good agreement with shock tube experiments in CO oxidation [16]. Although PG2 demonstrated better predictions for CH_4-O_2-Ar mixtures than all previous models, agreement is only fairly good with shock tube data for CH_4 mixtures [16]. Guiberti *et al.* [19] showed that the PG1 $CO_2(^1B_2)$ chemiluminescence mechanism [23] in laminar premixed conical CH_4/air and CO_2 or N_2 diluted flames was not even comparable to the overall mechanism for predicting the $CO_2(^1B_2)$ chemiluminescence profile and $CO_2(^1B_2)$ chemiluminescent intensity. Smirnov *et al.* [17] also obtained unsatisfactory results with the PG2 mechanism for the $CO_2(^1B_2)$/OH* chemiluminescent intensity ratios in premixed methane flames.

Recent $CO_2(^1B_2)$ chemiluminescence measurements in a shock tube [17] showed that the time history of $CO_2(^1B_2)$ chemiluminescence is closely contemporaneous with OH* chemiluminescence. Moreover, data in the literature [1,5] and our measurements in counterflow flame [24] have shown that the $CO_2(^1B_2)$/OH* chemiluminescent intensity ratio varies only slightly with equivalence ratio. These phenomena suggest that the CH + O_2 = $CO_2(^1B_2)$ + H reaction, which is also the main path of OH* generation in hydrocarbon flames (CH + O_2 = OH* + CO), dominates $CO_2(^1B_2)$ generation at the flame front. Recent results provided more information about $CO_2(^1B_2)$ and $CO_2(^3B_2)$ potential energy [25,26] and quantum yield [27], suggesting that the second $CO_2(^1B_2)$ chemiluminescence reaction scheme (R1, R2 and R4-R26) is closer to the chemistry of CO oxidation.

Since there is no available detailed $CO_2(^1B_2)$ chemiluminescence reaction mechanism based on the second scheme, and recent observations of the excited CO_2 molecule provided new physical insight, the purpose of the present study is to assemble a detailed $CO_2(^1B_2)$ chemiluminescence reaction mechanism based on the second scheme, which includes the CH + O_2 = $CO_2(^1B_2)$ + H reaction (R3), as the main $CO_2(^1B_2)$ formation path for hydrocarbon oxidation. In the following sections, the experimental apparatus and chemical modelling are described. The predicted results are evaluated against our opposed jet flame measurements and existing data in CO, CH_4 and C_2H_4 oxidation. Comparisons with the PG2 mechanism are also presented.

2. Chemiluminescent reaction kinetics

GRI-Mech 3.0 [28] (mechanism for fuel oxidation) was used for evaluating chemiluminescence mechanisms [2,9,10,12] for methane, ethylene and propane flames. We examined the USC-Mech II [29], UCSD mechanism [30] and CRECK C1-C3 + NOx mechanism [31–33] to ensure the robustness of the chemiluminescence sub mechanism, which is discussed later. An OH* chemiluminescence sub-mechanism, proposed by Kathrotia [12], with updated reaction rate constant for CH + O_2 = CO + OH* [10], was adopted as a tracer to anchor the $CO_2(^1B_2)$ chemiluminescent intensity. This sub-mechanism, with the GRI-Mech 3.0 mechanism, has been evaluated in [8,34]. The thermodynamic data for the sub-mechanism was from the Burcat database [35].

2.1. Thermodynamic data of $CO_2(^1B_2)$ and $CO_2(^3B_2)$.

The thermodynamic data of each species included specific heat (c_p^0), enthalpy (h^0), and entropy (s^0). In OPPDIF code [36], these three properties are expressed in NASA polynomial form [28,35]:

$$\frac{c_p^0}{R} = a_1 + a_2 T + a_3 T^2 + a_4 T^3 + a_5 T^4 \tag{1}$$

$$\frac{h^0}{R} = a_1 T + \frac{a_2 T^2}{2} + \frac{a_3 T^3}{3} + \frac{a_4 T^4}{4} + \frac{a_5 T^5}{5} + a_6 \tag{2}$$

$$\frac{s^0}{R} = a_1 \ln(T) + a_2 T + \frac{a_3 T^2}{2} + \frac{a_4 T^3}{3} + \frac{a_5 T^4}{4} + a_7 \tag{3}$$

where R is the universal gas constant, T is the gas temperature, a_1 to a_7 are the coefficients of the thermodynamic data's polynomial.

Because the $CO_2(^1B_2)$ and $CO_2(X^1\Sigma_g^+)$ share the same atoms, we assume that the specific heat of $CO_2(^1B_2)$ is that of its ground state $CO_2(X^1\Sigma_g^+)$. The mole entropy of $CO_2(^1B_2)$ is then the same value as $CO_2(X^1\Sigma_g^+)$ due to $s^0 = \int_0^T \frac{c_p^0(T)}{T} dT$. Based on these assumptions, the enthalpy (h^0) is the only unknown property. If we assume that the mean energy difference between $CO_2(^1B_2)$ and $CO_2(X^1\Sigma_g^+)$, denoted by ΔE, remains constant in the evaluated temperature range, the enthalpy of $CO_2(^1B_2)$ is calculated by $h^0_{CO2(1B2)} = h^0_{CO2(X1\Sigma+g)} + \Delta E$. Simulation from the literature [25] and [26] show that the range of $\Delta E_{CO2(1B2)}$ is from 5.60 to 6.63 eV (220 to 190 nm). Thus, by employing 5.60 eV as the $\Delta E_{CO2(1B2)}$, $a_6 = 1.7068E + 4$ between 200 and 1000 K and $1.6414E + 4$ between 1000 and 6000 K is calculated by Newton iterations. By using the same method, $\Delta E_{CO2(3B2)} = 3.55$ eV (350 nm) is employed from Ibraguimova *et al.* [26] to calculate a_6 for $CO_2(^3B_2)$. The results are $a_6 = -7.2374E + 03$ between 200 and 1000 K and $7.8909E + 03$ for 1000 to 6000 K.

2.2. $CO_2(^1B_2)$ reaction kinetics in hydrocarbon oxidation.

The proposed reactions responsible for $CO_2(^1B_2)$ formation in hydrocarbon oxidation are O + CO + M = $CO_2(^3B_2)$ + M (R1), $CO_2(^3B_2)$ -> $CO_2(^1B_2)$ (R2) and CH + O_2 = $CO_2(^1B_2)$ + H (R3) as shown in Table 1. The three-body recombination reaction (R1) corresponds to the $CO_2(^3B_2)$ formation through CO. The reaction rate constant was estimated from the reaction rate constants of R1 in the PG2 mechanism [16]. The pre-exponential factor (A) was fitted based on $CO_2(^1B_2)$ chemiluminescence intensity time history profile for CH_4 mixture from Petersen *et al.* [22] and $CO_2(^1B_2)$/OH* chemiluminescent ratios for CH_4-air mixture. E_a is kept the same in R1 as in [16] to preserve the $CO_2(^1B_2)$ temperature dependence for CO oxidations. The reaction rate constant of inter-system crossing reaction (R2) is estimated from very short fluorescence lifetime observation (no more than 5 ns) from CO_2 LIF measurement [27]. The main $CO_2(^1B_2)$ formation path in hydrocarbon oxidations, proposed by the current study, is R3. Its reaction rate constant was determined by the $CO_2(^1B_2)$/OH* chemiluminescent intensity

Table 1

Reaction mechanism for $CO_2(^1B_2)$; the reaction rate constant is presented in $k = A\,T^n\,\exp(-E_a\,/\,RT)$ with the units of $A\ (cm^3,\ mole,\ s)$, $E_a\ (kJ,\ mole)$.

No.	Reaction	A	n	E_a	Note
R1	$O + CO + M = CO_2(^3B_2) + M$	1.0E+13	0	10	this work, est. from [16]
	$H_2/2.0/\ H_2O/12/\ CO/1.75/\ CO_2/3.6/\ Ar/0.7/$				
R2	$CO_2(^3B_2) \rightarrow CO_2(^1B_2)$	2.0E+08	0	0	est. from [27,39]
R3	$CH + O_2 = CO_2(^1B_2) + H$	8.0E+10	0	0	this work
R4	$CO_2(^1B_2) \rightarrow CO_2 + h\nu$	1.0E+05	0	0	est. from CS_2[38] and NO_2[37]
R5	$CO_2(^3B_2) + Ar = CO_2 + Ar$	8.4E+10	0.5	0	est. from [16] and [27]
R6	$CO_2(^3B_2) + H_2O = CO_2 + H_2O$	8.4E+10	0.5	0	est. from [16] and [27]
R7	$CO_2(^3B_2) + CO_2 = CO_2 + CO_2$	9.1E+10	0.5	0	est. from [16] and [27]
R8	$CO_2(^3B_2) + CO = CO_2 + CO$	9.7E+10	0.5	0	est. from [16] and [27]
R9	$CO_2(^3B_2) + H = CO_2 + H$	3.1E+11	0.5	0	est. from [16] and [27]
R10	$CO_2(^3B_2) + H_2 = CO_2 + H_2$	2.7E+11	0.5	0	est. from [16] and [27]
R11	$CO_2(^3B_2) + O_2 = CO_2 + O_2$	8.8E+10	0.5	0	est. from [16] and [27]
R12	$CO_2(^3B_2) + O = CO_2 + O$	9.8E+10	0.5	0	est. from [16] and [27]
R13	$CO_2(^3B_2) + OH = CO_2 + OH$	9.9E+10	0.5	0	est. from [16] and [27]
R14	$CO_2(^3B_2) + CH_4 = CO_2 + CH_4$	1.2E+11	0.5	0	est. from [16] and [27]
R15	$CO_2(^3B_2) + N_2 = CO_2 + N_2$	1.0E+11	0.5	0	est. from [16] and [27]
R16	$CO_2(^1B_2) + Ar = CO_2 + Ar$	8.4E+10	0.5	0	0.01 of [16]
R17	$CO_2(^1B_2) + H_2O = CO_2 + H_2O$	8.4E+10	0.5	0	0.01 of [16]
R18	$CO_2(^1B_2) + CO_2 = CO_2 + CO_2$	9.1E+10	0.5	0	0.01 of [16]
R19	$CO_2(^1B_2) + CO = CO_2 + CO$	9.7E+10	0.5	0	0.01 of [16]
R20	$CO_2(^1B_2) + H = CO_2 + H$	3.1E+11	0.5	0	0.01 of [16]
R21	$CO_2(^1B_2) + H_2 = CO_2 + H_2$	2.7E+11	0.5	0	0.01 of [16]
R22	$CO_2(^1B_2) + O_2 = CO_2 + O_2$	8.8E+10	0.5	0	0.01 of [16]
R23	$CO_2(^1B_2) + O = CO_2 + O$	9.8E+10	0.5	0	0.01 of [16]
R24	$CO_2(^1B_2) + OH = CO_2 + OH$	9.9E+10	0.5	0	0.01 of [16]
R25	$CO_2(^1B_2) + CH_4 = CO_2 + CH_4$	1.2E+11	0.5	0	0.01 of [16]
R26	$CO_2(^1B_2) + N_2 = CO_2 + N_2$	1.0E+11	0.5	0	0.01 of [16]

ratio presented here, $CO_2(^1B_2)$ chemiluminescent intensity time history and $CO_2(^1B_2)$ dependence on temperature in shock tube measurements [22]. The radiative quenching from $CO_2(^1B_2)$ to $CO_2(X^1\Sigma_g^+)$ is described by R4. Because the inter-system crossing is very effective, direct measurement of $CO_2(^1B_2)$ lifetime is not possible. Thus, the lifetime of $NO_2(^2B_1)$ [37] and $CS_2(^1B_2)$ [38] was used to estimate $CO_2(^1B_2)$ radiative quenching lifetime. Therefore, a 25–40 μs lifetime for $NO_2(^2B_1)$ $(O(-5)s)$ and 2–13 μs lifetime for $CS_2(^1B_2)$ $(O(-6)toO(-5)s)$ were used to estimate that $CO_2(^1B_2)$ lifetime is $O(-5)s$. It should be noted that this methodology may underestimate k_4. The collisional quenching processes of $CO_2(^3B_2)$ and $CO_2(^1B_2)$ are presented by reaction R5 to R15 and R16 to R26 respectively. Their reaction rates were evaluated as 0.01 of the gas-kinetic frequency factor proposed in the PG1 mechanism [23]. The 0.01 factor was selected from suggestion of [17,27].

3. Experimental

The counterflow burner used to measure the $CO_2(^1B_2)$/OH* flame chemiluminescent intensity ratios was described previously [8]. Therefore, only a brief discission is presented here. As shown in Fig. 1, it consists of two identical, vertically opposed contracting nozzles with inner diameter of 30 mm, separated by a distance of 30 mm (H = 30 mm). Methane and air were injected into the chamber upstream of the accelerating nozzles, where they impinged on round plates to ensure adequate premixing before the nozzles. The two opposed nozzles were carefully aligned to ensure uniform and symmetric velocity profiles at the nozzle exit. The annular duct around the central pipe supplies nitrogen (N_2) coaxially to the central premixed fuel–air mixture. N_2 was introduced in the annulus through four side inlets, passed through a honeycomb mesh, and flowed through an annular ring surrounding the main nozzle. The N_2 co-flows were used to extinguish the secondary diffusion flames, formed away from the central flat flame and ensure the premixed flames were detached from the rims at the exit nozzle.

The equivalence ratio (φ) of the methane-air and propane-air mixtures was varied from 0.6 to 1.4, and the area averaged bulk velocity of the mixture at the jet exit, V_0, was varied from 1.8 to 6 m/s, which corresponded to a global flow strain rate range of 120 to 400 s^{-1}. The calculation of the strain rate, a, was based on the area averaged bulk velocity, V_0, as $a = 2\,V^0/H$ where H is the separation distance between the two pipes delivering the counterflow jets. The methane-air mixture outlet temperature was within a range of 300 ± 5 K. The equivalence
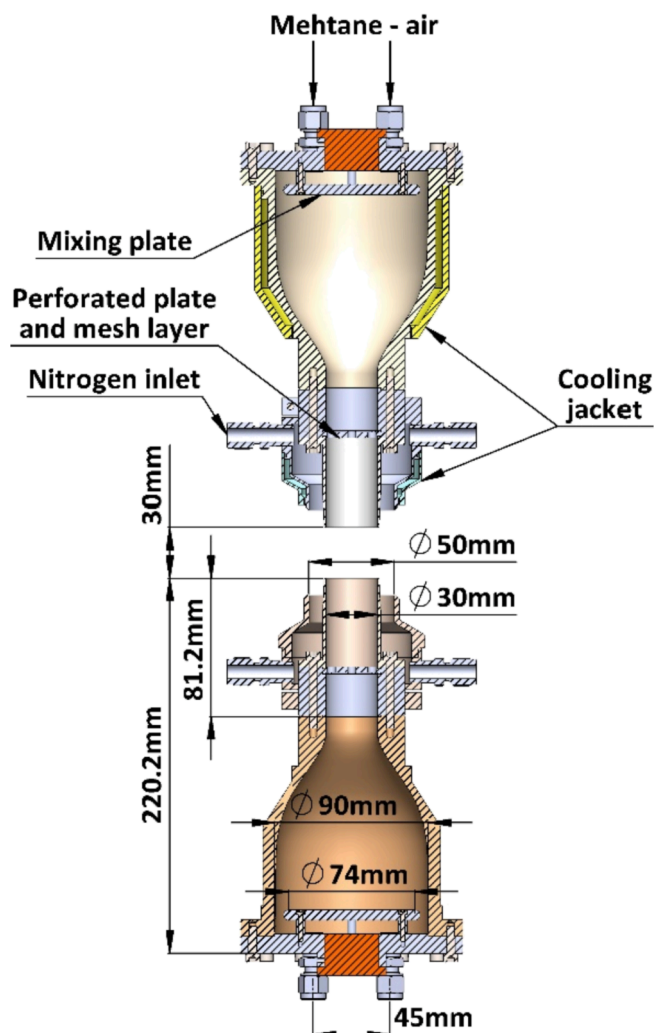

Fig. 1. Arrangement and dimensions of the counterflow burner.

ratio, strain rate and fuel conditions of the premixed hydrocarbon-air opposed flames are shown in the shadowed part of Table 2. The flame was operated at 1 atm.

The $CO_2(^1B_2)$/OH* chemiluminescent intensity ratios were measured by combined fibre-lens detection optics and an Echelle spectrograph. The light was collected by a UV fused silica plano-convex lens and focused on a UV-grade optical fibre with core diameter of 1500 µm. The collected light was directed to a 25 µm × 50 µm slit, fitted on an Echelle spectrograph (Andor Mechelle ME5000). The spectra of the detected light were recorded by an Intensified CCD camera (Andor DH-534). To minimize statistical uncertainties, 300 images, exposed over a second, were averaged. This spectrally resolved, line of sight, detection system provided a wavelength range from 250 to 800 nm with resolution of $\Delta \lambda \approx \lambda/4000$ nm. The measured flame spectra were processed to remove contributions from OH*, CH*(A), CH*(B) and C_2*. The resulting spectra were interpolated, using a polynomial, to obtain the $CO_2(^1B_2)$ chemiluminescent intensity at the location of the removed intensities. These full wavelength range $CO_2(^1B_2)$ chemiluminescence data were also used to remove the $CO_2(^1B_2)$ contribution to measured OH* chemiluminescence. Finally, a 250 – 690 nm integrated $CO_2(^1B_2)$ chemiluminescent intensity and a 305–325 nm integrated OH* chemiluminescent intensity, without the $CO_2(^1B_2)$ chemiluminescent intensity contribution, were used to calculate the $CO_2(^1B_2)$/OH* chemiluminescent intensity ratios for different equivalence ratios, strain rates and fuels. The uncertainty of chemiluminescent intensity ratio measurement is 14%, resulting in a 32% uncertainty of k_3 as evaluated by a sum of square roots method. A detailed uncertainty analysis is available in Supplemental Material 4.

4. Modelling

The final mechanism includes reactions of hydrocarbon oxidation and reactions describing formation and consumption of excited species. The mechanism includes 57 species and 363 reactions. The full reaction mechanism and thermodynamic data are listed as Supplemental Material 2 and 3.

The modelling of opposed flames (OPPDIF code [36]) had 10^{-13} absolute tolerance and 10^{-6} relative tolerance. A typical number of final mesh points was 500 for gradient and curvature adaptive grid control. The inlet flow conditions were according to the experimental conditions, whereas the equivalence ratio and strain rate range were varied more than the experiment, as shown by the non-shadowed part of Table 2.

For the modelling of the shock tube experiments, the Senkin code [40] was employed, based on a constant enthalpy and constant pressure assumption. Thus, the flow and mixture conditions for the shock tube modelling were those of the literature. Five H_2-N_2O-CO-Ar mixtures of the literature [16], noted as Mix 0 to Mix 4, were employed to assess R1 and R2. A CH_4-O_2-Ar mixture and a C_2H_4-O_2-Ar mixture of the literature [22] and [17] assessed the reaction R3. A full list of conditions and mixture compositions can be found in Supplemental Material 1. The ROP of radiative reactions (R4) for excited species is used as the modelled chemiluminescent intensity.

To further examine the performance and robustness of the proposed $CO_2(^1B_2)$ mechanism, we conducted $CO_2(^1B_2)$ rate of production and sensitivity analysis as shown in Fig. 2 For the methane mixture at low pressure, as shown in the Fig. 2 (a) and (c), the leading edge and peak of the $CO_2(^1B_2)$ time history are mainly attributed to R3. while the trailing edge and long tail of the $CO_2(^1B_2)$ time history are attributed to R1 -> R2 path. This is expected since CH is mainly formatted in the ignition front and CO is in abundance in the post ignition front region. The $CO_2(^1B_2)$ rate of production also indicates that only using the CO + O path is not able to accurately predict $CO_2(^1B_2)$ in hydrocarbon flames. Therefore, the mechanism proposed in this study can provide much improved prediction comparing with CO + O global mechanism. Fig. 2 (b) and (d) show that the peak $CO_2(^1B_2)$ mole fraction is only sensitive to R3 (formation) and R5 (argon collisional quenching) from the $CO_2(^1B_2)$ sub-mechanism. For the elevated pressure case, R1 and R2 become more critical than R3 in the prediction of $CO_2(^1B_2)$ time history as shown in Fig. 2 (e) and (g). The R3 path is the main contributor of the leading edge of the $CO_2(^1B_2)$ peak, while R1 - R2 path is the main contributor of the trailing edge. The peak value of the $CO_2(^1B_2)$ is governed by the R1 - R2 path. Similar to the low pressure case, the $CO_2(^1B_2)$ peak is mainly sensitive to the reactions from the proposed $CO_2(^1B_2)$ sub mechanism.

5. Results and discussion

5.1. $CO_2(^1B_2)$ chemiluminescent intensity time Histories.

Selected time histories of $CO_2(^1B_2)$ chemiluminescent intensity for Mix 0 to Mix 3 at low pressures are presented in Fig. 2. Both PG2 and the proposed model agreed well with the experimental $CO_2(^1B_2)$ chemiluminescent intensity time history. For all cases, the PG2 mechanism slightly overpredicted the leading edge and underpredicted the trailing edge by up to 30% (Fig. 2a). However, the new mechanism reduces the under prediction of the trailing edge to less than 5% relative to experimental data (Fig. 2a). Since the observation time of the shock tube experiment was short [16], the trailing edge intensity profile is a stricter criterion than the leading edge intensity when assessing the $CO_2(^1B_2)$ mechanism. This is because a slight under prediction of the trailing edge $CO_2(^1B_2)$ intensity for these time cases will lead to very large disparity between experiment and prediction if the observation time is sufficiently long. Therefore, based on this criterion, the new model provided a much better prediction.

To further examine the performance of the new $CO_2(^1B_2)$ chemiluminescence model for H_2-N_2O-CO-Ar mixtures, two elevated pressure tests for Mix 0 were performed (Fig. 3). For the lower temperature case, shown in Fig. 3a, the new and PG2 models over predicted the $CO_2(^1B_2)$ intensity at the leading and trailing edges. The peak intensity occurred at a slightly later time for the new model than for the PG1 model. Since the peak time of the experimental results is hard to detect, the comparison of the performance of the two models is ambiguous. However, for the higher temperature case, the deviation between PG2 prediction and experiment is more than 300% at 200 µs, at the trailing edge $CO_2(^1B_2)$ intensity. The new model performed much better at the trailing edge and the difference between new model and experiment is less than 30% at 200 µs. Overall, the ability of the new mechanism to predict elevated pressure trends is much improved.

For the CH_4-based mixture, low and elevated pressure cases were utilized to assess the available $CO_2(^1B_2)$ models. Fig. 4a shows promising agreement between the low pressure experiment of Petersen *et al.* [22] and the new $CO_2(^1B_2)$ model. However, the PG2 model over predicted by a factor of two the $CO_2(^1B_2)$ in the tail region (after 400 µs region). For the elevated pressure case, both models performed similarly in tracing the $CO_2(^1B_2)$ time history: the models tend to predict thinner $CO_2(^1B_2)$ chemiluminescent intensity profiles than the experiment [22].

In higher hydrocarbon, C2 and C3, flames, $CO_2(^1B_2)$ is more prominent than in methane flames [15]. Thus, two shock tube experiments for C_2H_4-based mixture [17] were employed to examine the performance of

Table 2
Flame Conditions.

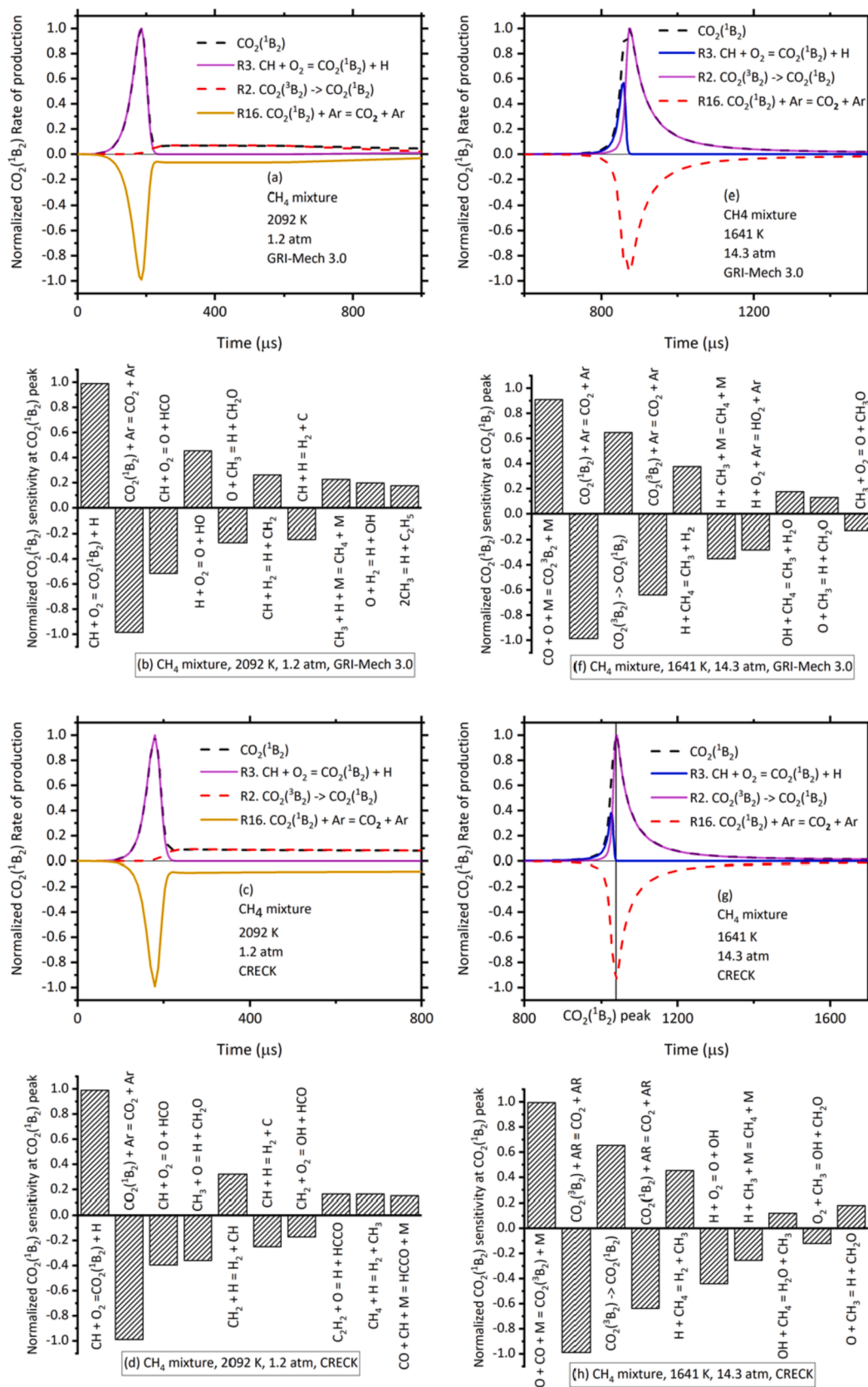| φ | Strain rate (s^{-1}) | | | | |
	120	160	240	320	400
0.6	CH_4	CH_4	CH_4	CH_4	CH_4
0.7	CH_4	CH_4/C_3H_8	CH_4/C_3H_8	CH_4	CH_4
0.8	CH_4	CH_4/C_3H_8	CH_4/C_3H_8	CH_4/C_3H_8	CH_4/C_3H_8
0.9	CH_4	CH_4/C_3H_8	CH_4/C_3H_8	CH_4/C_3H_8	CH_4/C_3H_8
1.0	CH_4	CH_4/C_3H_8	CH_4/C_3H_8	CH_4/C_3H_8	CH_4/C_3H_8
1.1	CH_4	CH_4/C_3H_8	CH_4/C_3H_8	CH_4/C_3H_8	CH_4/C_3H_8
1.2	CH_4	CH_4/C_3H_8	CH_4/C_3H_8	CH_4/C_3H_8	CH_4/C_3H_8
1.3	CH_4	CH_4/C_3H_8	CH_4/C_3H_8	C_3H_8	C_3H_8
1.4	C_3H_8	C_3H_8	C_3H_8	C_3H_8	C_3H_8

Fig. 2. Normalized $CO_2(^1B_2)$ rate of production and sensitivity analysis at low and elevated pressure for CH_4 mixture, predicted by GRI-Mech 3.0 based model and CRECK based model.
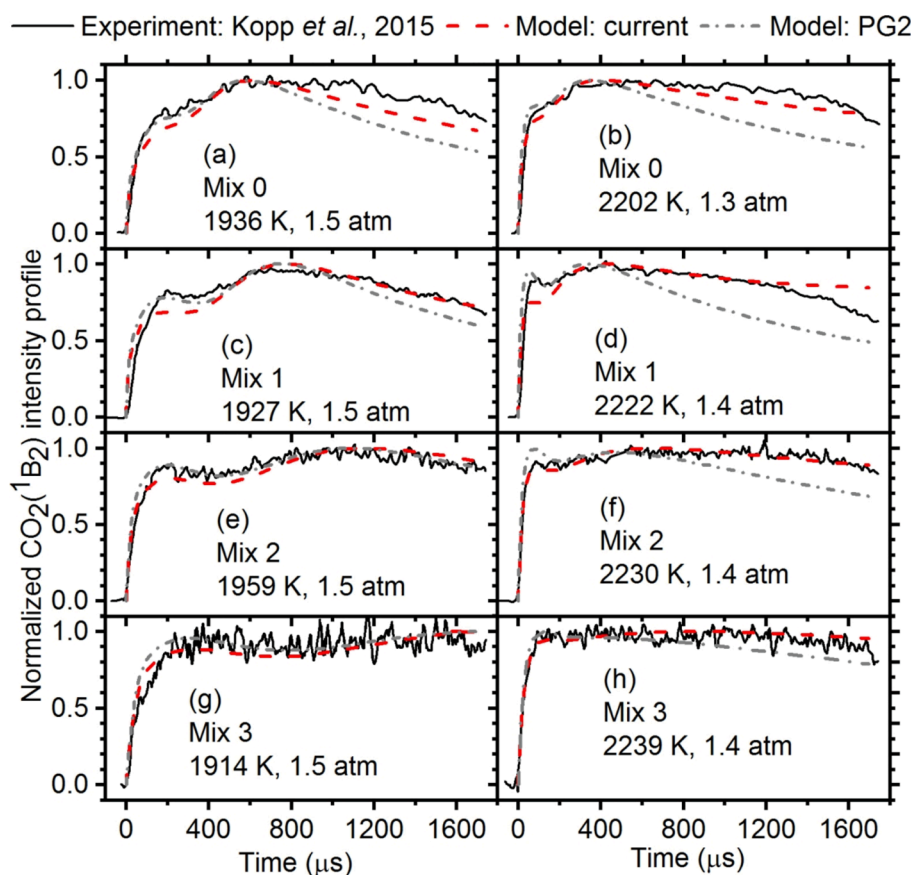
Fig. 3. Normalized $CO_2(^1B_2)$ intensity profiles for H_2-N_2O-CO-Ar mixtures at low pressures, measured in a shock tube (black line), predicted by the new model (red dash line) and predicted by the PG2 model (grey dash dot line). (For interpretation of the references to colour in this figure legend, the reader is referred to the web version of this article.)
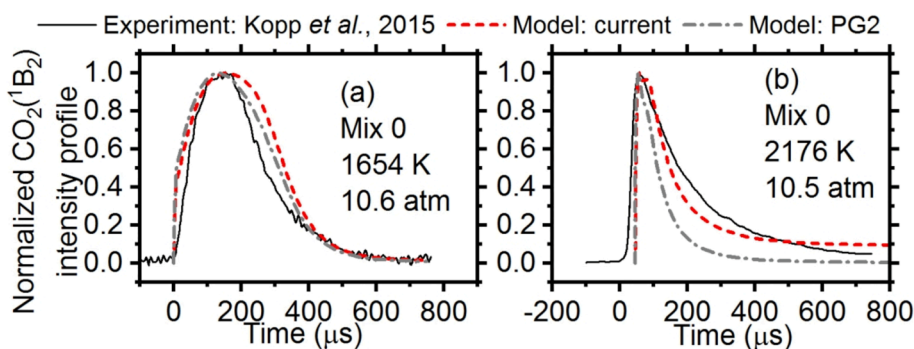

Fig. 4. Normalized $CO_2(^1B_2)$ intensity profiles for Mix 0 at elevated pressures, measured in a shock tube [16] (black line), predicted by the current model (red dash line) and predicted by the PG2 model (grey dash dot line). The predicted profile in (b) was shifted in time to align with the peak of measured profile[41]. (For interpretation of the references to colour in this figure legend, the reader is referred to the web version of this article.)

$CO_2(^1B_2)$ models. Comparison shows quite good agreement between the new model and experiment, whereas the PG2 model over predicted the $CO_2(^1B_2)$ in the tail regions and did not reproduce the peak shape for the low temperature case (Fig. 5). This ability of the new mechanism to accurately predict the $CO_2(^1B_2)$ time history in C_2H_4-based mixtures supports the selection of reaction R1 as the main formation path in hydrocarbon oxidation.

5.2. Temperature dependence of peak $CO_2(^1B_2)$ chemiluminescent intensity Magnitude.

The temperature dependence of peak $CO_2(^1B_2)$ chemiluminescent intensity magnitude for five different H_2-N_2O-CO-Ar mixtures is shown in Fig. 6. Although the E_a of the R1 of the new model is the same as that of corresponding reaction of PG2, the new model slightly under predicted the peak $CO_2(^1B_2)$ chemiluminescent intensity for the low temperature and pressure cases. This under prediction is caused by the different $CO_2(^1B_2)$ enthalpy of the two mechanisms ($\Delta E = 4.14\,eV$ for PG2, as calculated by the a6 in the supplied material of [16]). Since the measured $CO_2(^1B_2)$ intensity profile for H_2-N_2O-CO-Ar mixtures at low pressure showed a double hump shape rather than a sharp peak (Fig. 2), the authors suggest that an integrated $CO_2(^1B_2)$ intensity over sufficient time could be a better criterion. As discussed earlier, the new model could better predict the trailing edge of the $CO_2(^1B_2)$ time history
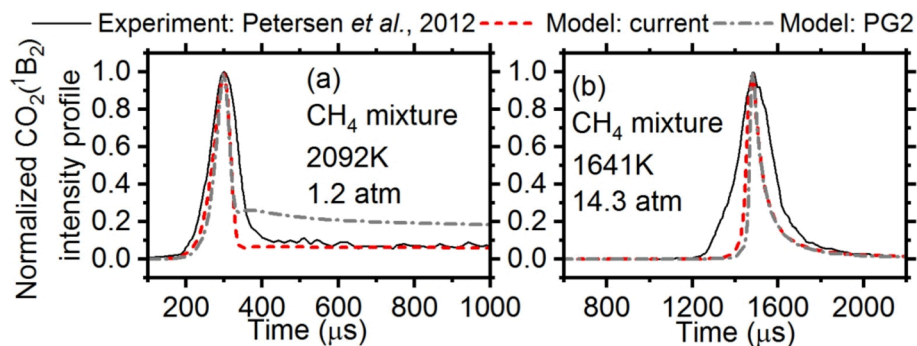
Fig. 5. Normalized $CO_2(^1B_2)$ intensity profiles for CH_4 mixture at low and elevated pressures, measured in a shock tube [22] (black line), predicted by the current model (red dash line) and predicted by the PG2 model (grey dash dot line). These two predicted profiles were shifted in time to align with the peak of measured profile [41]. (For interpretation of the references to colour in this figure legend, the reader is referred to the web version of this article.)

Fig. 6. Normalized $CO_2(^1B_2)$ intensity profiles for C_2H_4 mixture at low pressure, measured in a shock tube [17] (black line), predicted by the current model (red dash line) and predicted by the PG2 model (grey dash dot line). These two predicted profiles were shifted in time to align with the peak of measured profile [41]. (For interpretation of the references to colour in this figure legend, the reader is referred to the web version of this article.)
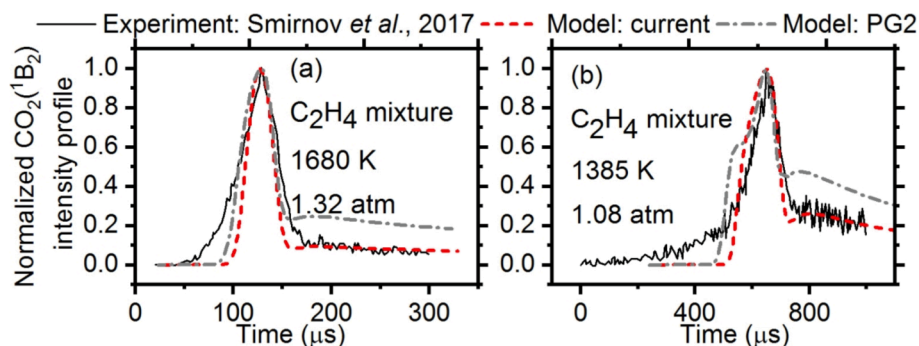

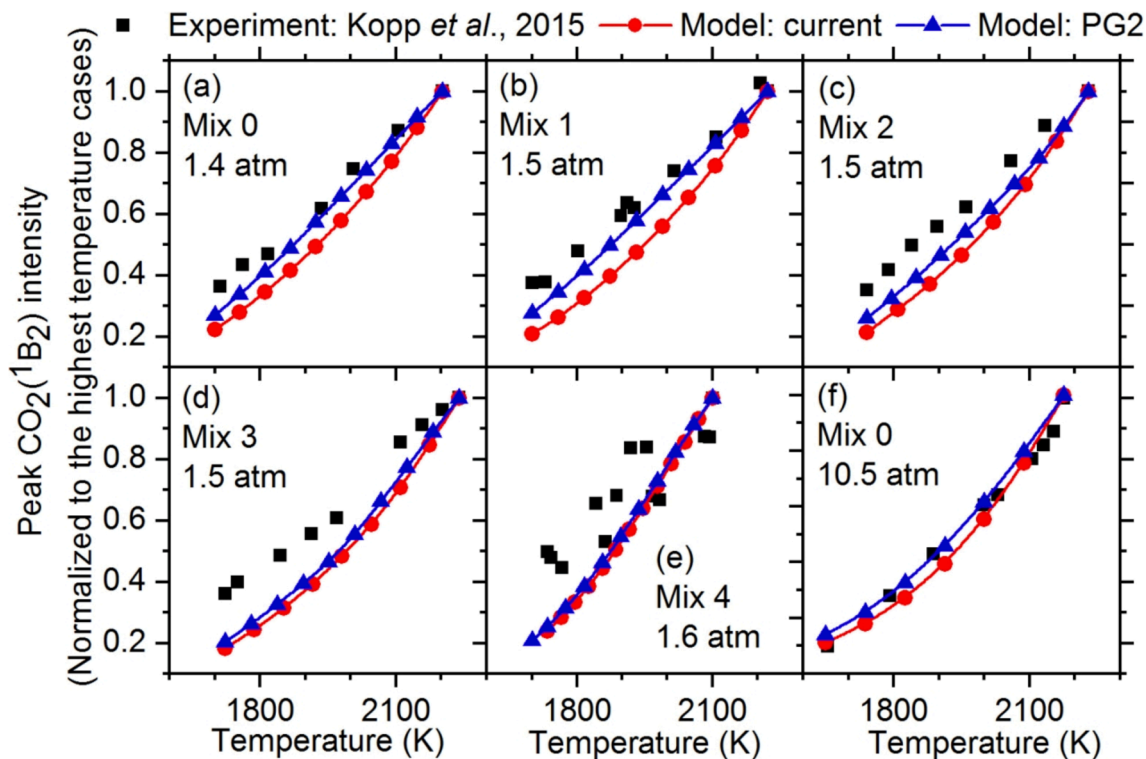**Fig. 7.** Normalized peak intensity for $CO_2(^1B_2)$ from experiments [16] compared with mechanism predictions for Mix 0 (a), Mix 1 (b), Mix 2 (c), Mix 3 (d), and Mix 4 (e) at low pressure and for Mix 0 (f) at elevated pressure. The data and predictions are plotted as a function of their initial temperature.

profile. Thus, better agreement can be expected for sufficient time integrated $CO_2(^1B_2)$ intensity cases. This conjecture can be tested in the elevated pressure cases. Fig. 3 shows the $CO_2(^1B_2)$ time history profile with a prominent peak shape, which suggests that using the peak intensity is a more appropriate assessment criterion. Therefore, as shown in Fig. 6f, the agreement between new and PG2 models and experiment is quite good.

For the methane based mixture, the new mechanism captured the experimental trends (Fig. 7). For the low pressure case, the new mechanism over predicted the measured peak $CO_2(^1B_2)$ intensity by less than 30%, while the PG2 model over predicted it by a factor of more than 2.5 and did not capture the trends well. Moreover, for the elevated pressure case, although there is about 50% difference between the new model and measurement, the new model can capture the trends well. In contrast, there is a large over prediction (between 250% and 500%) of the data by the PG2 model.

This ability of the proposed new mechanism to reproduce the measured $CO_2(^1B_2)$ peak intensity and time history profile of different hydrocarbon and CO based mixtures in shock tube experiments suggest that the current model is reliable, at least at low pressure. The reaction rate constant of R3 is competent to describe the $CO_2(^1B_2)$ temperature dependence. Thus, a further examination of the current $CO_2(^1B_2)$ model was performed in the counterflow burner flames to examine the equivalence ratio dependence of the $CO_2(^1B_2)$/OH* chemiluminescent intensity ratio.

5.3. $CO_2(^1B_2)$/OH* chemiluminescent intensity ratios.

The value of the narrow bandpass filtered chemiluminescent intensity ratio of $CO_2(^1B_2)$/OH* tends to be independent of equivalence ratio in methane flames [5]. However, full spectral range based $CO_2(^1B_2)$/OH* chemiluminescent intensity ratio measurements are still not available in the literature. Thus, the first objective of this part is to fill this gap. A good agreement with experimental data for the $CO_2(^1B_2)$/OH* chemiluminescent intensity ratio needs accurate prediction of both $CO_2(^1B_2)$ and OH*. Therefore, $CO_2(^1B_2)$/OH* chemiluminescent intensity ratio can be used as a strict criterion for assessing the combined $CO_2(^1B_2)$ chemiluminescence sub-mechanism and the fuel oxidation mechanism. The OH* chemiluminescence mechanism of the current study is the same as in the literature [3,12,34] and can be used as a reference marker for evaluating $CO_2(^1B_2)$ mechanisms.

The predicted and measured $CO_2(^1B_2)$/OH* chemiluminescent intensity ratios for CH_4-air and C_3H_8-air flames as a function of equivalence ratio are illustrated in Fig. 8. For the methane flames, the measured $CO_2(^1B_2)$/OH* chemiluminescent intensity ratio showed a 'W' shape trend against equivalence ratio: it decreased from 6.6 to 3.7 for φ = 0.6 and φ = 0.7, increased to 5.6 at stoichiometric point, then decreased to 4.7 at φ = 1.1, and finally increased to 6.0 at φ = 1.3. The cases predicted by the new model precisely described this 'W' shape

variation and the largest quantitative difference is less than 30% (φ = 1.3). In contrast, the PG2 model failed both qualitatively and quantitatively the prediction of $CO_2(^1B_2)$/OH* chemiluminescent intensity ratio. The PG2 predictions showed a monotonic decrease and the magnitude was about one order higher than experimental results (φ = 0.6). For the propane-air flames, the $CO_2(^1B_2)$/OH* chemiluminescent intensity ratio was about two times higher than for methane flames. The experimental data increased by 13%, from φ = 0.7 to φ = 1.0, and then decreased 20% from φ = 1.0 to φ = 1.4. The comparison between the computed data by the new mechanism and the measurement is promising. Except at φ = 0.7, the trend was captured, while the new model under predicted the magnitude by 50% (Fig. 8b). The larger difference between experimental and predicted data may be due to the fuel oxidation mechanism. Several studies have shown that the ability of GRI-Mech 3.0 in predicting propane flames, especially for predicting chemiluminescence, is not satisfactory [12,42]. However, the GP2 mechanism failed to predict the trend, while the predicted magnitude was still far from the experimental data. Although the combined GRI-Mech 3.0 + OH* sub-mechanism and $CO_2(^1B_2)$ sub-mechanism did not fully predict the propane flame, as shown in Fig. 9, the new $CO_2(^1B_2)$ sub-mechanism and its combination with GRI-Mech 3.0 mechanism could be used for predicting the $CO_2(^1B_2)$ for natural gas blend flames.

6. Conclusions

The kinetics of $CO_2(^1B_2)$ formation were studied by combining modelling and shock tube and opposed jet burner experiments. The shock tube data were for H_2-N_2O-CO-Ar mixtures [16], CH_4-O_2-Ar mixture [22] and C_2H_4-O_2-Ar mixture [17]. The premixed opposed jet flame experiment was for equivalence ratio range of 0.6 to 1.3 for CH_4-air flames and 0.7 to 1.4 for C_3H_8-air flames for strain rate range of 160 to 400 s^{-1}.

A new $CO_2(^1B_2)$ chemiluminescence mechanism, including the intersystem crossing reaction and a novel $CO_2(^1B_2)$ generation path for hydrocarbon oxidation, was proposed for the first time. The reaction rate constant of $CO + O + M = CO_2(^3B_2) + M$ (R1) was determined within $\pm$ 60% uncertainty based on available experimental data for H_2-N_2O-CO-Ar mixtures as:

$k_1 = 1 \times 10^{13}$ exp(-10 / RT) cm^6 mol^2 s^{-1}, KJ mol^{-1}.

The reaction rate constant of $CH + O_2 = CO_2(^1B_2) + H$ (R3) was determined within $\pm$ 32% uncertainty based on the CH_4-O_2-Ar mixture shock tube experimental data and $CO_2(^1B_2)$/OH* chemiluminescent intensity ratio data in premixed CH_4 flames as:

$k_3 = 8 \times 10^{10}$ cm^3 mol^{-1} s^{-1}.

This novel $CO_2(^1B_2)$ chemiluminescence mechanism performs much better in predicting $CO_2(^1B_2)$ chemiluminescence behaviour for H_2-N_2O-CO-Ar mixtures, CH_4-O_2-Ar mixture and C_2H_4-O_2-Ar mixture than previous mechanisms. Further assessment was conducted by adopting the $CO_2(^1B_2)$/OH* chemiluminescent intensity ratio in premixed CH_4 and

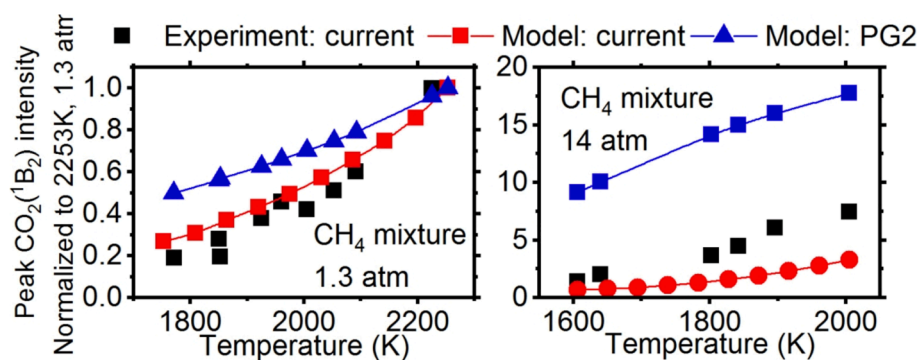**Fig. 8.** Normalized peak intensity for $CO_2(^1B_2)$ from experiments [22] compared to mechanism predictions for CH_4 based mixture at low and elevated pressures. The data and predictions are plotted as a function of their initial temperature.
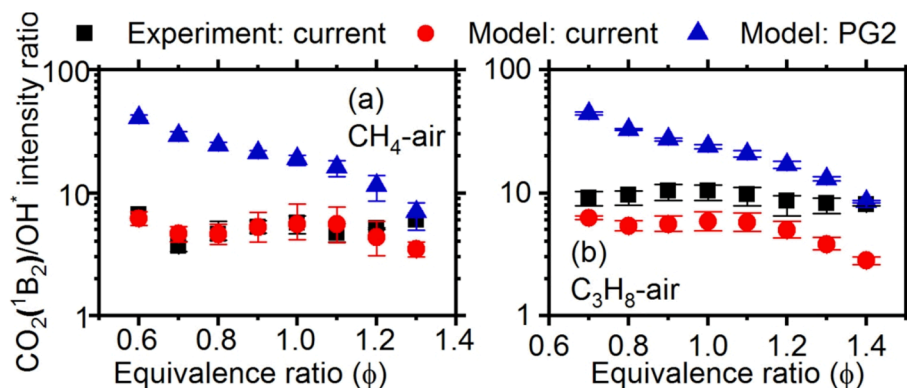
Fig. 9. $CO_2(^1B_2)$/OH* chemiluminescent intensity ratios for CH_4-air and C_3H_8-air flames as a function of equivalence ratio. The error bars refer to the upper and lower limit of the data for different strain rates. The data are plotted in semi logarithmic coordinate.

C_3H_8 opposed jet flames as a stricter criterion. The new model along with GRI-Mech 3.0 can provide very good prediction of the $CO_2(^1B_2)$/OH* chemiluminescent intensity ratio for CH_4-air flames and fair prediction for C_3H_8-air flames.

Declaration of Competing Interest

The authors declare that they have no known competing financial interests or personal relationships that could have appeared to influence the work reported in this paper.

Acknowledgments

References

[1] Hardalupas Y, Orain M. Local measurements of the time-dependent heat release rate and equivalence ratio using chemiluminescent emission from a flame. Combust Flame 2004;139(3):188–207.

[2] Smith GP, Park C, Schneiderman J, Luque J. C2 Swan band laser-induced fluorescence and chemiluminescence in low-pressure hydrocarbon flames. Combust Flame 2005;141(1-2):66–77.

[3] Panoutsos C, Hardalupas Y, Taylor A. Numerical evaluation of equivalence ratio measurement using OH* and CH* chemiluminescence in premixed and non-premixed methane–air flames. Combust Flame 2009;156(2):273–91.

[4] Guethe F, Guyot D, Singla G, Noiray N, Schuermans B. Chemiluminescence as diagnostic tool in the development of gas turbines. Appl Phys B 2012;107(3): 619–36.

[5] Nori V, Seitzman J, Evaluation of chemiluminescence as a combustion diagnostic under varying operating conditions, in 46th AIAA Aerospace Sciences Meeting and Exhibit.. The American Institute of Aeronautics and Astronautics: Reno. U.S.: Nevada; 2008.

[6] Hardalupas Y, Panoutsos CS, Taylor AMKP. Spatial resolution of a chemiluminescence sensor for local heat-release rate and equivalence ratio measurements in a model gas turbine combustor. Exp Fluids 2010;49(4):883–909.

[7] Garcia-Armingol T, Ballester J. Flame chemiluminescence in premixed combustion of hydrogen-enriched fuels. Int J Hydrogen Energy 2014;39(21):11299–307.

[8] Liu Y, et al. Experimental and Numerical Study of Chemiluminescence Characteristics in Premixed Counterflow Flames of Methane based Fuel blends. Grapevine, Texas, U.S: The American Institute of Aeronautics and Astronautics; 2017.

[9] Smith GP, Park C, Luque J. A note on chemiluminescence in low-pressure hydrogen and methane-nitrous oxide flames. Combust Flame 2005;140(4):385–9.

[10] Bozkurt M, Fikri M, Schulz C. Investigation of the kinetics of OH* and CH* chemiluminescence in hydrocarbon oxidation behind reflected shock waves. Appl Phys B 2012;107(3):515–27.

[11] Carl S, Van Poppel M, Peeters J. Identification of the CH+ O2→ OH (A)+ CO Reaction as the Source of OH (AX) Chemiluminescence in C2H2/O/H/O2 Atomic Flames and Determination of its Absolute Rate Constant over the Range T= 296 to 511 K. J Phys Chem A 2003;107(50):11001–7.

[12] Kathrotia T. Reaction kinetics modeling of OH*, CH*, and C2* chemiluminescence. Germany: Ruprecht-Karls-Universität Heidelberg; 2011.

[13] Gaydon, A.G., *The spectroscopy of flames*. Spaceflight. Vol. 1. 1957, London: Chapman and Hall.

[14] Kaskan W. The source of the continuum in carbon monoxide hydrogen-air flames. Combust Flame 1959;3:39–48.

[15] Samaniego JM, Egolfopoulos FN, Bowman CT. CO2* chemiluminescence in premixed flames. Combust Sci Technol 1995;109(1–6):183–203.

[16] Kopp MM, Mathieu O, Petersen EL. Rate Determination of the CO2* Chemiluminescence Reaction CO+ O+ M⇄ CO2*+ M. Int J Chem Kinet 2015;47 (1):50–72.

[17] Smirnov VN, Tereza AM, Vlasov PA, Zhiltsova IV. Luminescent Characteristics of the Shock-Wave Ignition of an Ethylene− Oxygen Mixture. Combust Sci Technol 2017;189(5):854–68.

[18] Zimmer L, et al. Evaluation of chemiluminescence as sensor for lean premixed combustion. Continuum 2003;387:p. 431.4.

[19] Guiberti T, Durox D, Schuller T. Flame chemiluminescence from CO2-and N2-diluted laminar CH4/air premixed flames. Combust Flame 2017;181:110–22.

[20] Kaufman F, Laffitte P, Clyne MAA, Thrush BA. The kinetics of the carbon monoxide flame bands. Symp (Int) Combust 1963;9(1):177–83.

[21] Donald Leslie Baulch, D.D.D., J. Duxbury, S. J. Grant, *Evaluated Kinetic Data for High Temperature Reactions, Vol. 3: Homogeneous Gas Phase Reactions of the 02-03 System, the CO-02-HZ System and of Sulphur Containing Species.* Vol. 3. 1976, London: Butterworths. 593.

[22] Petersen E, Kopp M, Donato N, Güthe F. Assessment of Current Chemiluminescence Kinetics Models at Engine Conditions. J Eng Gas Turbines Power 2012;134(5): 051501.

[23] Kopp M, et al. CO2* chemiluminescence study at low and elevated pressures. Appl Phys B 2012;107(3):529–38.

[24] Liu, Y., *Chemiluminescence and CO pollutant formation in premixed counterflow flames*, in *Mechanical Engineering*. 2019, Imperial College London: London, UK.

[25] Ibraguimova LB, Minaev BF. Analysis of Dissociation-Recombination Processes for the CO2 Molecule with the Spin-Orbit Coupling Taken into Account. Opt Spectrosc 2016;120(3):345–51.

[26] Ibraguimova LB, Minaev BF, Irgibaeva IS. Spin-orbit coupling and dissociation of CO2 molecules. Opt Spectrosc 2014;117(5):695–702.

[27] Lee T, Bessler WG, Yoo J, Schulz C, Jeffries JB, Hanson RK. Fluorescence quantum yield of carbon dioxide for quantitative UV laser-induced fluorescence in high-pressure flames. Appl Phys B 2008;93(2-3):677–85.

[28] Smith, G.P., et al. *GRI-Mech 3.0.* URL: http://www.me.berkeley.edu/gri_mech 1999 [cited 51; 55]. Available from: http://www.me.berkeley.edu/gri_mech.

[29] Wang, H., et al., *USC mech version II. High-temperature combustion reaction model of H2/CO/C1-C4 compounds.* 2007.

[30] Mechanism U. *Chemical-kinetic mechanisms for combustion applications*, in *Mechanical and Aerospace Engineering (Combustion Research)*. University of California at San Diego (http://combustionucsdedu) 2016.

[31] Ranzi E, Frassoldati A, Stagni A, Pelucchi M, Cuoci A, Faravelli T. Reduced kinetic schemes of complex reaction systems: fossil and biomass-derived transportation fuels. Int J Chem Kinet 2014;46(9):512–42.

[32] Ranzi E, Cavallotti C, Cuoci A, Frassoldati A, Pelucchi M, Faravelli T. New reaction classes in the kinetic modeling of low temperature oxidation of n-alkanes. Combust Flame 2015;162(5):1679–91.

[33] Bagheri G, Ranzi E, Pelucchi M, Parente A, Frassoldati A, Faravelli T. Comprehensive kinetic study of combustion technologies for low environmental impact: MILD and OXY-fuel combustion of methane. Combust Flame 2020;212: 142–55.

[34] Liu, Y., et al., *A numerical study on the ability to predict the heat release rate, equivalence ratio and NO emission using chemiluminescence in counterflow premixed methane flames*, in *8th European Combustion Meeting*. 2017, The Combustion Institute: Dubrovnik, Croatia.

[35] Burcat, A. and B. Ruscic. *Ideal gas thermodynamic data in polynomial form for combustion and air pollution use.* Available from: The latest version of this database is available by anonymous FTP from ftp://ftp.technion.ac.il/pub/supported/ aetdd/thermodynamics. There is a web-based mirror, http://garfield.chem.elte.

hu/Burcat/burcat.html, in Europe.(2004-1997)(cited 20 December 2008) 2007; Available from: http://garfield.chem.elte.hu/Burcat/burcat.html.

[36] Lutz AE, et al. OPPDIF: A Fortran program for computing opposed-flow diffusion flames. Livermore, CA (United States): Sandia National Labs; 1997.

[37] Sugimoto N, Takezawa S, Takeuchi N. Rotational analysis and radiative lifetime measurement on the 2B1 ($K' = 0$) excited state of NO2 with v′ 2= 6, 7, 8, and 9. J Mol Spectrosc 1983;102(2):372–83.

[38] Weyh T, Demtroder W. Lifetime measurements of selectively excited rovibrational levels of the V B-1(2) state of CS2. J Chem Phys 1996;104(18):6938–48.

[39] Lin M, Bauer S. Bimolecular Reaction of N2O with CO and the Recombination of O and CO as Studied in a Single-Pulse Shock Tube. J Chem Phys 1969;50(8):3377–91.

[40] Lutz AE, Kee RJ, Miller JA. SENKIN: A FORTRAN program for predicting homogeneous gas phase chemical kinetics with sensitivity analysis. Livermore, CA (USA): Sandia National Labs; 1988.

[41] Dryer FL, Haas FM, Santner J, Farouk TI, Chaos M. Interpreting chemical kinetics from complex reaction–advection–diffusion systems: Modeling of flow reactors and related experiments. Prog Energy Combust Sci 2014;44:19–39.

[42] Lowry W, de Vries J, Krejci M, Petersen E, Serinyel Z, Metcalfe W, et al. Laminar flame speed measurements and modeling of pure alkanes and alkane blends at elevated pressures. J Eng Gas Turbines Power 2011;133(9):091501.